Achieving superior fatigue strength in a powder-metallurgy titanium alloy via

in-situ globularization during hot isostatic pressing

- 3 R.P. Guo^{a,1}, Min Cheng^{a,1}, C.J. Zhang^a, J.W. Qiao^a, C. Cai^b, Z.B. Zhao^c, L. Xu^c, D.S. Xu^c, R. Yang^c,
- 4 Y.S. Shi^b, and P.K. Liaw^d
- ^aCollege of Materials Science and Engineering, Taiyuan University of Technology, Taiyuan 030024,
- 6 China

1

2

- ⁷ State Key Laboratory of Materials Processing and Die & Mould Technology, Huazhong University
- 8 of Science and Technology, Wuhan 430074, China
- ^o Institute of Metal Research, Chinese Academy of Sciences, Shenyang 110016, China
- ^dDepartment of Materials Science and Engineering, The University of Tennessee, 37996–2200
- 11 Knoxville, TN, USA
- 12 The authors contributed equally to the work.

14 Abstract:

13

15

16

17

18

19

20

21

22

Powder-metallurgy (PM) titanium alloys exhibit outstanding quasistatic-mechanical properties, but suffer from low fatigue performance, which severely limits their applications in aerospace. Here, we achieve a superior fatigue strength of 600 MPa in a near- α PM titanium alloy, using a two-step hot-isostatic-pressing scheme, during which more than 80 vol. % (volume fraction) randomly orientated equiaxed grains was obtained. The largely improved fatigue strength (~ 25%) is mainly attributed to the *in-situ* globularization of the lamella-like microstructure, leading to higher crack nucleation resistance and lower growth rates of short cracks. The present findings offer a useful route for fabricating PM titanium alloys with high fatigue strengths.

23

24

25

Keywords: Titanium alloys; Hot isostatic pressing; Globularization; Fatigue strength; Fatigue-crack initiation

26

27

28

29

Titanium alloys are promising structural materials for crucial load-bearing components in the modern aerospace due to their excellent comprehensive mechanical properties [1–4]. Powder hot isostatic pressing (HIP) allows near-net-shape manufacturing of large-size and thin-wall components

with complex structures [5–9]. The quasistatic mechanical properties of powder-HIPed titanium alloy components can be comparable to or even better than those of as-forged ones [10–14]. However, some of these components still suffer from low high-cycle fatigue (HCF) strengths [12,13,15], which needs to be substantially improved for aerospace-industrial applications.

Compared with the as-forged alloys, the defects, such as porosity, can significantly decrease the fatigue life of the as-sintered titanium alloys [16,17], and the fatigue data are more scattered due to the competition for the fatigue failure from pores and microstructures [19,20]. HIP is known to be an advanced powder-metallurgy technique, which can make compacts approach nearly full densities (> 99.7%) [10,12]. Our recent work [21] has demonstrated that the pore size in the HIPed Ti-6Al-4V was less than the critical defect size below, which the residual micropores would not become involved in the fatigue-crack initiation and decrease the fatigue-endurance limit. Hence, tailoring the microstructure is one of the most effective routes to enhance the fatigue limit of powder-HIPed titanium alloy components, which can alter the crack-initiation modes.

In the case of the HIPed Ti-6Al-4V, the microstructure consists of equiaxed α and lamellar α + β phases [13], which is quite different from the as-cast and as-forged microstructures. Generally speaking, the fully equiaxed microstructure with a fine grain size has a higher HCF strength than the lamellar colony microstructure due to the higher resistance to crack growth [22]. Reduction in the total strain energy and microdefects are the driving forces for the globularization of colony microstructures in the as-forged alloys. Stefansson and Semiatin [23] reported that the lamellar colonies in the as-cast alloys possess relatively high stability, and the globularization cannot be accomplished in the absence of plastic deformation only by the heat treatment. Recent studies [24,25] reported that the tangled dislocations in the additively manufactured Ti-6Al-4V could induce the formation of substructure boundaries after multi-step heat treatments, initiating the globularization of martensitic laths. Herein, the aim of this study is to design a new HIP schedule to promote the *in-situ* globularization of a lamellar microstructure, and to improve the HCF strengths of HIPed alloys.

In the present work, a two-step HIP procedure was proposed, where the first-step HIP was maintained at a low $(\alpha + \beta)$ phase regime to generate enough stored energy and deformation-induced dislocation substructures, and the second-step HIP was conducted at a high $(\alpha + \beta)$ phase regime to accelerate the recrystallization and globularization. The globularization mechanism and large improvement of HCF limits were discussed. These findings provide useful guidance to regulating the microstructure and enhancing the fatigue limit of powder-HIPed titanium alloy components.

The gas-atomized Ti55 powder with a chemical composition of Ti-5.41Al-3.46Sn-2.91Zr-0.67Mo-0.28Si-0.36Nb-0.41Ta-0.08O (weight percent, wt.%) was employed as a starting material. Two HIP schedules, HIP1 and HIP2, were shown in Fig. 1a, and the corresponding HIPed samples were defined as S1 and S2, respectively. HIP1 was 940°C/140MPa/3h, and HIP2 differed from HIP1 in which S2 was firstly HIPed at 880 °C/140 MPa for 1 h before being heated up to 940°C and then HIPed under identical pressure for another 2 h. The pretreatment process for HIP was described in our previous work [26, 27]. The phase diagram of Ti55 was calculated, using the Pandat software [28], and the β transus was 1,005 °C (Fig. 1b). The mass transport and interface motion facilitate the powder consolidation [29]. A high HIP temperature can accelerate the mass transport, but may decrease the interface motion, such as recrystallization, since the β phase shows the fast dynamic recovery and little strain hardening [30]. The final HIP temperature of 940 °C was chosen for the Ti55 powder in order to ensure the presence of enough α phase in which the strain could be accumulated and recrystallization would take place during powder densification.

Microstructural characterization of the HIPed Ti55 was carried out, using scanning electron microscopy (SEM, FEI Quanta650) equipped with an electron backscatter diffraction (EBSD) system and transmission electron microscopy (TEM, JEM-2100F) combined with energy-dispersive X-ray spectroscopy. The volume fractions of equiaxed grains were measured by the Image-Pro Plus software [21]. The metallurgical samples for EBSD were ground, polished, and electrolytically etched, using a reagent of 59% CH₃OH + 35% C₄H₁₀O + 6% HClO₄ (vol.%) at - 30 °C and a current density of 1

mA/cm². The TEM foils were prepared by the ion-beam thinning technique.

Tensile samples with a diameter of 5 mm and a gauge length of 25 mm were measured on a Zwick Z050 testing machine. Three samples were tested for each condition. The tension-tension HCF tests were conducted on an Amsler axial resonance pulser with a frequency of 80 Hz and a stress ratio *R* of 0.1. Dogbone-fatigue specimens with a minimum cross-sectional diameter of 4.5 mm, and a nylon cloth polished surface finish were used.

The microstructure of the sample after the first step of HIP2 mainly consists of elongated α and β phases (Fig. S1). In Fig. 1c, some equiaxed grains were already observed at the original particle boundaries due to the local recrystallization. Interestingly, several fine equiaxed grains could also be found within the original coarse powder, and the globularization mechanisms, such as boundary splitting and local shearing, can be confirmed (Figs. 1c and d). In Fig. 1e, particles of the S2-type silicide can effectively pin the dislocations and enhance the formation of dislocation-induced substructures, which in turn increases the total strain energy and breaks the original lamellae forming the fine equiaxed grains. It can be deduced that enough strain energy has been accumulated, and microdefects have been formed after the first-step HIP, which provides the probability to induce complete globularization during the second-step HIP.

The microstructure of the sample S1 is composed of the lamella-like and equiaxed α phase and a little β phase (Fig. 2a). The grain size of the equiaxed α phase is about 8 μ m, and the thickness of α lamellae is about 2 μ m. For sample S1, the volume fraction of equiaxed grains is only about 25%, because the interfacial coherency of the α/β phase boundary limits the globularized fraction. By contrast, the globularized fraction of the sample S2 is more than 80%, and the grain size of the equiaxed α phase is about 10 μ m (Fig. 2d).

The powder rearrangement, plastic yielding, creeping, and bonding contribute to the powder densification during HIP [31]. Given the applied HIP temperature and pressure, HIP of the encapsulated powder can be considered as a special thermomechanical processing (TMP) [12]. In

HIP2, the first-step HIP consists of the deformation and initial stage of annealing, and the second-step HIP is an effectively annealing, which allows the globularization. A high strain energy can enhance the globularization of the colony microstructure during TMP [32]. Li *et al.* [33] calculated the total strain energy in the different HIP routes of Ti-6Al-4V compacts. It was demonstrated that the largest strain energy could be accumulated, using the HIP route (the pressure raised first and then the temperature elevated). In the HIP2 scheme of the present work, the first-step HIP enlarges the contribution of plastic yielding to the powder densification, leading to a higher driving force for the following recrystallization and globularization. In addition, the dwell time at 940 °C is shorter (Fig. 1a), while the microstructure is coarser in S2. This trend is consistent with the conclusion that more strain energy has been generated during HIP2, based on the kinetic of the static globularization [34].

The EBSD analysis of the randomly selected areas of the HIPed compacts along the stress-axis direction was conducted to investigate the crystallographic aspects related to the local equiaxed grains and lamellae, as also shown in Fig. 2. The maximum index of S1 (23.3) is much higher than that of S2 (6.4), indicating a high degree of microtextures with the basal plane (Fig. 2c). Thus, although the microstructure of the HIPed titanium-alloy compacts is isotropic and shows almost no obvious texture at the mesoscale [13,36], there are several locations of microtextured regions showing the near basal orientation in S1.

The globularization mechanism of S2 is described in Fig. 2g. Before the first-step HIP, the martensitic α' phase decomposes to α and β lamellae, and the colony, α , generally tends to present similar orientations [37,38]. The first-step HIP can generate the strain energy, dislocation-induced substructures, and crystal defects in the α lamellae, which is good for the further dynamic recrystallization and globularization. During the second-step HIP, the termination migration and the boundaries splitting caused by recovery promote the transformation of the α colony inside the original powder particle into a globular morphology. It is also noted that \sim 40 vol.% of the α phase can be obtained (Fig. 1b), and the recrystallization in the high ($\alpha + \beta$) phase regime can change the

morphology of the initial α/β interfaces [39]. The recrystallization of prior β grains breaks the orientation relationship between α and β phases [40], and the grain-boundary sliding and the strain partitioning may occur (Fig. 2d), leading to the more random orientation of equiaxed α grains (Fig. 2f). Therefore, the coexistence of multiple mechanisms improves the globularized fraction of the lamella-like microstructure.

The tensile data of Ti55 alloys were listed in Table S1. The tensile strength of S2 (955 MPa) is similar to that of S1 (975 MPa). The stress-fatigue life (S-N) curves showed that with the increase of the fatigue life (N_f), the maximum applied stress decreases continuously (Fig. 3a). There are two fracture modes for the failed fatigue samples. When the maximum applied stress is high, the fatigue cracks initiate at the surface or subsurface areas. With the decrease of the maximum applied stress, the fatigue cracks start to initiate at the interior. The fatigue strength of S2 is about 600 MPa, which is $\sim 25\%$ higher than that of S1 (480 MPa) and even higher than that of the wrought Ti600 [41]. A comparison of the fatigue and tensile strengths between S2 and other high-temperature titanium alloys was exhibited in Fig. 3b [17,19, 41–59]. Almost the maximum fatigue efficiency (the ratio of fatigue to tensile strengths) has achieved for S2, demonstrating the superior fatigue property of S2,

The fractographic analysis has been conducted to clarify the fatigue behavior (Fig. S2), and the results revealed that the dominant characteristic at the crack-initiation sites is the formation of facets. The facet size is larger than the thickness of lamellae and the size of equiaxed grains. Prasada et al. [35] confirmed that the facet was the (0001) plane, using EBSD with the tilt correction technique. The fatigue cracks of failure samples may initiate at the lamella-like microstructure or equiaxed grains with similar near the basal orientation.

It is a basic understanding that the fatigue-crack initiation consists of the formation of planarslip bands, the crack nucleation, and early propagation along these slip bands. When the short crack reaches a certain size, the crack grows rapidly until fatigue failure. Cracking along the slip bands results in the formation of facets due to the transgranular fracture of the α phase [60,61]. Recently, Stinville *et al.* [62] unveiled the physical origins of fatigue strengths and found that the amplitude of the early slip localization events after the first cycle determines the fatigue strength, and the fatigue efficiency decreases with the increasing slip location amplitude. In Fig. S3, the striations on the facet surfaces resemble the slip steps. The mean slip location amplitude during fatigue-crack initiation is $200 \sim 300$ nm for S2, and $275 \sim 510$ nm for S1. Therefore, the fatigue-endurance limit at 10^7 cycles of S2 is expected to be higher than that of S1.

The fatigue-crack nucleation and early-stage propagation consume more than 90% of the total fatigue life in HCF, depending on the stress level [63]. The fine granular area (FGA) at the fatigue-initiation sites can be regarded as a crack, and the model for the formation of FGA based on the plastic zone at the crack tip has been established [64]. The plastic-zone size of a short crack can be calculated by [65]:

$$r_{\rm p} = \frac{(1-2\nu)^2}{\pi} \frac{(\Delta K_{\rm ini})^2}{(\sigma_{\rm v})^2} \tag{1}$$

where v, σ_y , and ΔK_{ini} are the Poisson ratio (0.31), yield strength, and stress intensity factor at the tip of a crack, respectively.

According to the fracture morphologies of samples with the $N_{\rm f}$ in the range of $2 \times 10^6 \sim 10^7$ cycles, the fatigue cracks initiate at the interior. The $\Delta K_{\rm ini}$ can be calculated by [66]:

171
$$\Delta K_{\rm ini} = 0.65 \Delta \sigma \sqrt{\pi \sqrt{area_{\rm ini}}}$$
 (2)

where $\Delta \sigma$ is the maximum applied stress, and $\sqrt{\text{area}_{\text{ini}}}$ is the Murakami parameter, which is the size of the FGA. In the present work, the value of ΔK_{ini} is in the range of 11.4 – 11.8 MPa·m^{1/2} for S1 and S2. The r_p value calculated is about 7.5 μ m, which is close to the mean size of the equiaxed α grains.

The mechanism modeling of the fatigue-crack initiation for HIPed Ti55 compacts is illustrated in Fig. 4. The microstructure plays a main role in influencing fatigue damage. The slip length in the equiaxed grains is much larger, compared with α lamellae, which is beneficial for the dislocation multiplication and motion. Therefore, the dislocation pileups at the interfaces of α lamellae are much denser than at the grain boundaries of equiaxed grains under the same $N_{\rm f}$, leading to the earlier

nucleation of a microcrack in S1.

Serval α lamellae may simultaneously suffer from the fatigue damage caused by the local plastic deformation after the nucleation of a microcrack since the r_p value is larger than the thickness of α lamellae. Additionally, a local microtexture on the (0001) plane is available (Fig. 2c). The α lamellar cluster with the similar near basal orientation is more appropriate for the growth of a short crack than a single α lamella. Therefore, the short cracks in S1 grow relatively fast. However, the equiaxed grains present more random orientations than the lamella-like microstructures (Fig. 2f). When a short crack reaches another equiaxed grain rather than an α cluster, more dislocations will be piled up at the grain boundaries until the applied resolved shear stress can make the dislocation slip along the (0001) plane [67]. This trend can be also demonstrated by the fatigue-crack-initiation site of S2 being rougher than that of S1 (Fig. S2). Thus, the higher resistance for the fatigue-microcrack nucleation and lower growth rate of short cracks increase the fatigue life of S2.

In summary, a PM Ti55 alloy with a superior fatigue strength (600 MPa) has been obtained, using a newly developed two-step HIP procedure. Enough strain energy and crystal defects formed during the first-step HIP can promote the *in-situ* globularization of the lamella-like microstructure during the second-step HIP. Compared with S1, the significantly enhanced fatigue strength (~ 25%) of S2 is attributed to the formation of the nearly full equiaxed structure with a random orientation, which increases the mean free path of dislocations during the crack nucleation and decreases the growth rate of short cracks. The present work paves the way for producing PM titanium-alloy components with tailored microstructures, superior fatigue strength, and excellent tensile properties for load-bearing applications.

Declaration of Competing Interest

The authors declare that they have no known competing financial interests or personal relationships that could have appeared to influence the work reported in this paper.

Acknowledgments

205

- This work was supported by the National Natural Science Foundation of China (Nos.
- 51905192, 52171122, and 52205407), the Natural Science Foundation of Shanxi Province, China (No.
- 208 202201D211085), and Anhui Provincial Key R&D Programmes (No. 202104a05020053). P. K. Liaw
- 209 very much appreciates the supports from the National Science Foundation (DMR 1611180, 1809640,
- and 2226508) with program directors, Drs. J. Madison, J. Yang, G. Shiflet, and D. Farkas.

211 **References**

- 212 [1] D. Banerjee, J.C. Williams, Acta Mater. 61 (2013) 844-879.
- 213 [2] L. Qi, S. He, C. Chen, B. Jiang, Y. Hao, H. Ye, R. Yang, K. Du, Acta Mater. 195 (2020) 151-162.
- 214 [3] L. Huang, Q. An, L. Geng, S. Wang, S. Jiang, X. Cui, R. Zhang, F. Sun, Y. Jiao, X. Chen, C. Wang, Adv.
- 215 Mater. 33 (2021) 2000688.
- 216 [4] Y. Chong, R. Zhang, M. S. Hooshmand, S. Zhao, D. C. Chrzan, M. Asta, J. W. Morris Jr, A. M. Minor,
- 217 Nat. Commun. 12 (2021) 6158.
- 218 [5] D.P. Delo, R.E. Dutton, S.L. Semiatin, H.R. Piehler, Acta Mater. 47 (1999) 3159-3167.
- 219 [6] Y.X. Yuan, J. Mei, V. Samarov, D. Seliverstov, X. Wu, J. Mater. Process. Technol. 182 (2007) 39-49.
- [7] S. Irukuvarghula, H. Hassanin, C. Cayron, M. Aristizabal, M.M. Attallah, M. Preuss, Acta Mater. 172
- 221 (2019) 6-17.
- 222 [8] M. Wang, Y. Lu, B. Pang, Z.T. Kloenne, H.L. Fraser, Y.L. Chiu, M.H. Loretto, Acta Mater. 173 (2019)
- 223 242-248.
- [9] I. Sen, S. Tamirisakandala, D.B. Miracle, U. Ramamurty, Acta Mater. 55 (2007) 4983-4993.
- 225 [10] G. Wegmann, R. Gerling, F. Schimansky, Acta Mater. 51 (2003) 741-752.
- 226 [11] S. Di Iorio, L. Briottet, E.F. Rauch, D. Guichard, Acta Mater., 55 (2007) 105-118.
- [12] Y. Lu, M. Aristizabal, X. Wang, B. Pang, Y.L. Chiu, Z.T. Kloenne, H.L. Fraser, M.H. Loretto, Acta Mater.
- 228 165 (2019) 520-527.
- 229 [13] K. Zhang, J. Mei, N. Wain, X. Wu, Metall. Mater. Trans. A 41 (2010) 1033-1045.
- 230 [14] R. Guo, L. Xu, J. Wu, R. Yang, B.Y. Zong, Mater. Sci. Eng. A 639 (2015) 327-334.

- 231 [15] C. Cai, B. Song, P. Xue, Q. Wei, J. Wu, W. Li, Y. Shi, J. Alloy. Compd. 686 (2016) 55-63.
- 232 [16] F. Cao, K.S. Ravi Chandran, Int. J. Fatigue 102 (2017) 48-58.
- 233 [17] P. Kumar, U. Ramamurty, Acta Mater. 173 (2019) 242-248.
- 234 [18] K.S. Ravi Chandran, Nat. Mater. 4 (2005) 303-308.
- 235 [19] L. Meng, J. Gao, J. Yue, J. Zhang, X. Zhao, D. Zhang, Mater. Sci. Eng. A 798 (2020) 140085.
- [20] F. Cao, P. Kumar, M. Koopman, C. Lin, Z. Zak Fang, K.S. Ravi Chandran, Mater. Sci. Eng. A 630 (2015)
- 237 139-145.
- 238 [21] M. Cheng, Z.G. Lu, J. Wu, R. Guo, J. Qiao, L. Xu, R. Yang, J. Mater. Sci. Technol. 98 (2022) 177-185.
- [22] G. Lütjering, J.C. Williams, Titanium, 2nd ed., Springer, Verlag Berlin Heidelberg, 2007.
- 240 [23] N. Stefansson, S.L. Semiatin, Metall. Mater. Trans. A 34 (2003) 691-698.
- 241 [24] R. Sabban, S. Bahl, K. Chatterjee, S. Suwas, Acta Mater. 162 (2019) 239-254.
- 242 [25] Z. Zhao, J. Chen, H. Tan, G. Zhang, X. Lin, W. Huang, Scripta Mater. 146 (2018) 187-191.
- 243 [26] M. Cheng, J. Wu, Z.G. Lu, R. Guo, L. Xu. R. Yang, Acta Metall. Sin. (Engl. Lett.) 24 (2021) 1386-1394.
- 244 [27] R. Guo, L. Xu, Z. Chen, Q. Wang, B.Y. Zong, R. Yang, Mater. Sci. Eng. A 706 (2017) 57-63.
- 245 [28] C. Yang, D. Hu, X. Wu, A. Huang, M. Dixon, Mater. Sci. Eng. A 534 (2012) 268-276.
- 246 [29] S. L. Chen, S. Daniel, F. Zhang, Y.A. Chang, X.Y. Yanb F.Y. Xie, R. Schmid-Fetze, W.A. Oates, Calphad
- 247 26 (2002)175-188.
- 248 [30] S.F. Liu, M.Q. Li, J. Luo, Z. Yang, Mater. Sci. Eng. A589 (2014) 15-22.
- 249 [31] D.P. Delo, H.R. Piehler, Acta Mater. 47 (1999) 2841-2852.
- 250 [32] J. Zhang, H. Li, M. Zhan, Manufacturing Rev. 7 (2020) 18.
- 251 [33] M. Li, C.V.S. Limb, R. Zou, X. An, D. Wang, Int. J. Mech. Sci. 196 (2021) 106288.
- 252 [33] N. Stefansson, S.L. Semiatin, D. Eylon, Metall. Mater. Trans. A 33 (2002) 3527-3534.
- 253 [35] K. Prasada, R. Sarkar, V. Singh, P. Ghosal, A. Bhattacharjee, H. Gokhale, Acta Mater. 218 (2021) 117214.
- 254 [36] C. Qiu, N.J.E. Adkins, H. Hassanin, M.M. Attallah, K. Essa, Mater. Des. 87 (2015) 845-853.
- 255 [37] F.R. Kaschel, R.K. Vijayaraghavan, A. Shmeliov, E.K. McCarthy, M. Canavan, P.J. McNally, D.P.
- 256 Dowling, V. Nicolosi, M. Celikin, Acta Mater. 188 (2020) 720-732.
- 257 [38] R. Guo, L. Xu, B.Y. Zong, R. Yang, Acta Metall. Sin. (Engl. Lett.) 30 (2017) 735-744.
- 258 [39] X.G. Fan, H.J. Zheng, Y. Zhang, Z.Q. Zhang, P.F. Gao, M. Zhan, J. Liu, Mater. Sci. Eng. A 720 (2018)

- 259 214-224.
- 260 [40] S. Balachandran, S. Kumar, D. Banerjee, Acta Mater. 131 (2017) 423-434.
- 261 [41] L. Zeng, Y. Zhao, Q. Hong, G. Yang, J. Alloys Compd. 509 (5) (2011) 2081-2086.
- 262 [42] M. Hagiwara, T. Kitaura, Y. Ono, T. Yuri, T. Ogata, O. Kanou, Mater. Trans. 53 (8) (2012) 1486-1494.
- 263 [43] N. Hrabe, T. Gnäupel-Herold, T. Quinn, Int. J. Fatigue 94 (2017) 202-210.
- 264 [44] G. Kasperovich, J. Hausmann, J. Mater. Process. Technol. 220 (2015) 202-214.
- 265 [45] S. Li, B. Xiong, S. Hui, W. Ye, Y. Yu, Mater. Sci. Eng. A 460-461 (2007) 140-145.
- 266 [46] Y.X. Liu, W. Chen, Z.Q. Li, B. Tang, X.Q. Han, G. Yao, Int. J. Fatigue 97 (2017) 79-87.
- 267 [47] M. Hagiwara, T. Kitashima, S. Emura, Mater. Sci. Eng. A 727 (2018) 43-50.
- 268 [48] X. Nie, W. He, S. Zang, X. Wang, J. Zhao, Surf. Coat. Technol. 253 (2014) 68-75.
- 269 [49] Y. Okazaki, E. Gotoh, Mater. Sci. Eng. C 31 (2) (2011) 325-333.
- 270 [50] A.L. Pilchak, Scr. Mater. 68 (5) (2013) 277-280.
- [51] A. Soltani-Tehrani, M. Habibnejad-Korayem, S. Shao, M. Haghshenas, N. Shamsaei, Addit. Manuf. 51
- 272 (2022) 102584.
- 273 [52] X. Song, L. Wang, M. Niinomi, M. Nakai, Y. Liu, M. Zhu, Mater. Sci. Eng. A 619 (2014) 112-118.
- [53] R.R.B. Svetlana G. Ivanova, and Richard D. Sisson Jr, JMEPEG (2002).
- 275 [54] M.N. Toshikazu Akahori, and Kei-Ichi Fukunaga, Metall. Mater. Trans. A (2000) 1937-1948.
- 276 [55] G.Q. Wu, C.L. Shi, W. Sha, A.X. Sha, H.R. Jiang, Mater. Des. 46 (2013) 668-674.
- 277 [56] H. Yu, F. Li, Z. Wang, X. Zeng, Int. J. Fatigue 120 (2019) 175-183.
- 278 [57] Y. Yue, L.Y. Dai, H. Zhong, X.Y. Zhang, S.X. Liang, M.Z. Ma, R.P. Liu, J. Alloys Compd. 696 (2017)
- 279 663-669.
- 280 [58] S. Zhang, W. Zeng, Q. Zhao, X. Gao, Q. Wang, J. Alloys Compd. 689 (2016) 114-122.
- 281 [59] P. Kumar, U. Ramamurty, Acta Mater. 194 (2020) 305-320.
- 282 [60] A.L. Pilchak, J.C. Williams, Metall. Mater. Trans. A 42 (2011) 1000-1027.
- [61] R.K. Nalla, B.L. Boyce, J.P. Campbell, J.O. Peters, R.O. Ritchie, Metall. Mater. Trans. A 33 (2002) 891-
- 284 918.
- 285 [62] J.C. Stinville, M.A. Charpagne, A. Cervellon, S. Hemery, F. Wang, P.G. Callahan, V. Valle, T.M. Pollock,
- 286 Science 377 (2022) 1065-1071.

[63] Y.S. Hong, Z.Q. Lei, C.Q. Sun, A.G. Zhao, Int. J. Fatigue 28 (2014) 144-151. [64] O. Takeshi, S. Stanzl-Tschegg, B.M. Schoenbauer, Eng. Fract. Mech. 115 (2014) 241-254. [65] Y. Murakami, Metal Fatigue: Effects of Small Defects and Nonmetallic Inclusions. London: [66] R.W. Hertzberg, R.P. Vinci, J.L. Hertzberg, Deformation and Fracture Mechanics of Engineering Materials, fifth ed., Wiley, Hoboken, 2012. [67] W.J. Evans, M.R. Bache, Int. J. Fatigue 16 (1994) 443-52.

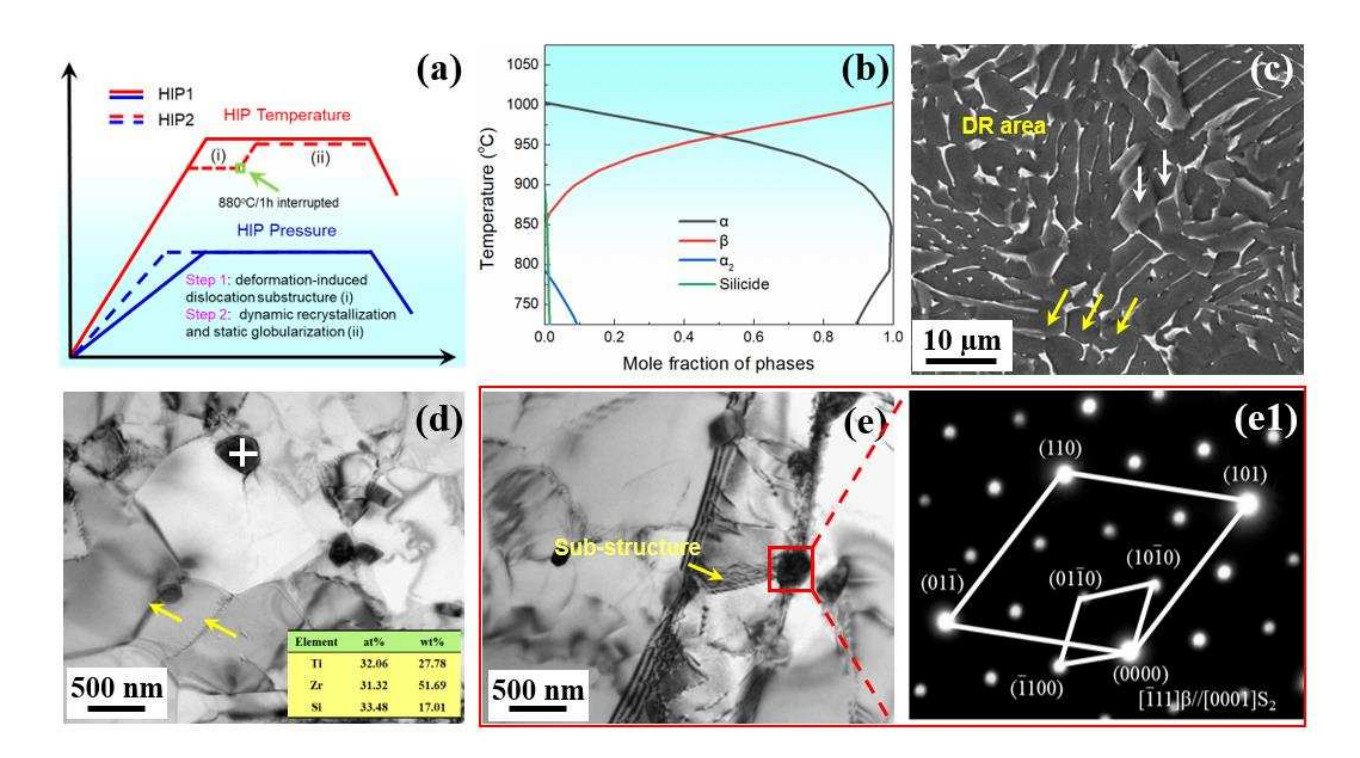


Fig.1 HIP procedures and microstructures of the Ti55 alloy after interrupted HIP2. (a) Schematic diagram of HIP1 and HIP2 procedures. (b) Ti55-alloy phase diagram calculated with the Pandat software. (c-e) shows the microstructure of the sample S2 after the first step of HIP2. (c) SEM image, the arrows indicating the fine equiaxed grains, and DR standing for dynamic recrystallization. (d) TEM bright-field image showing the formation of equiaxed grains and the inset table showing the chemical composition of the silicide indicated by a white plus sign. (e) TEM bright-field image presenting the dislocation substructure developed during HIP and corresponding selected area electron diffraction pattern of the silicide and β phase (e1).

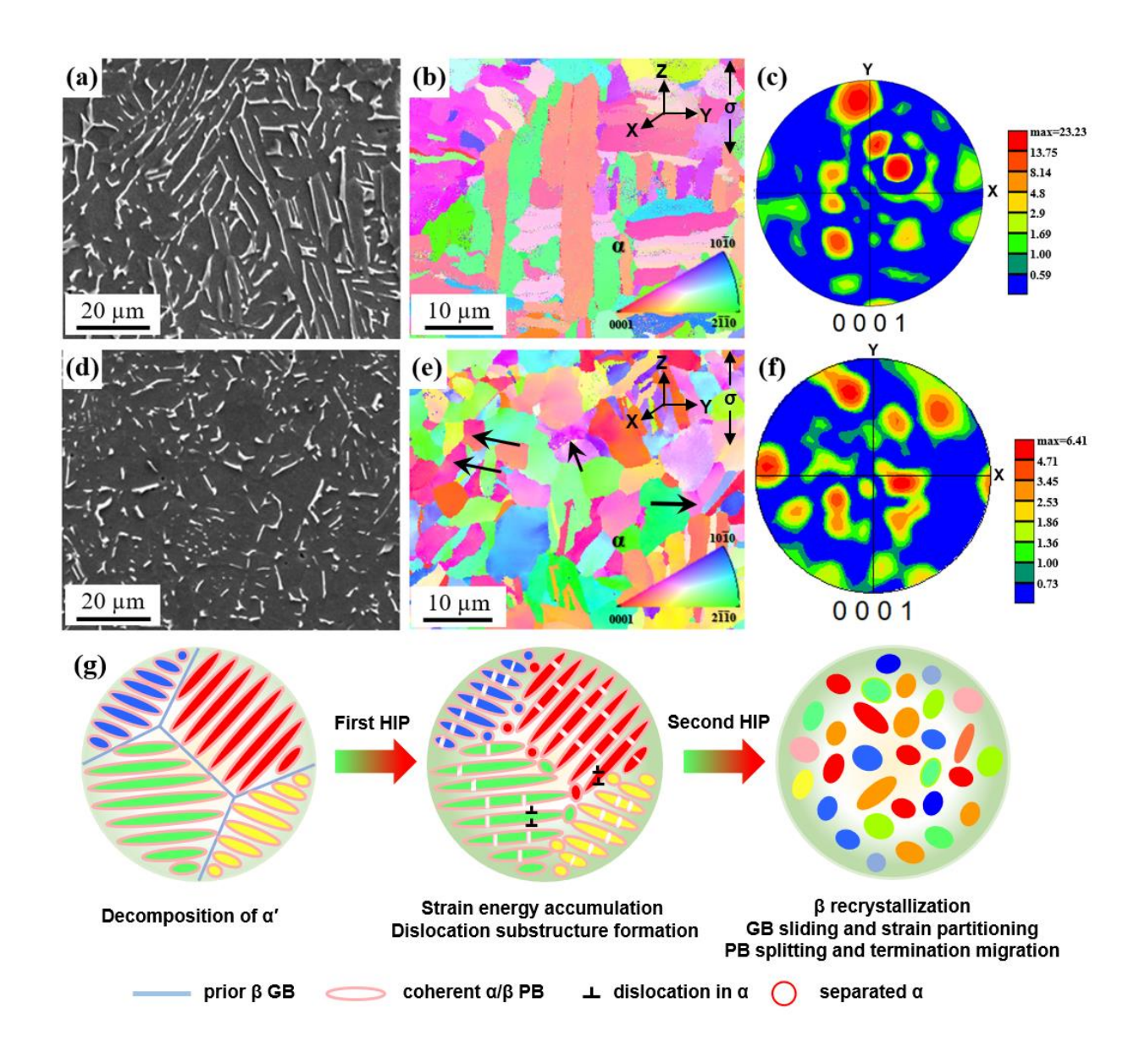


Fig. 2 Microstructures and formation mechanisms. (a-c) S1 and (d-f) S2. (a, d) SEM images. (b, e) EBSD inverse pole-figure maps taken along the stress-axis direction, the arrows presenting the boundary splitting and termination migration. (c,f) EBSD pole-figure maps. (g) Schematic diagrams illustrating the *in-situ* globularization mechanism of α lamellae during HIP2. GB – grain boundary, PB – phase boundary.

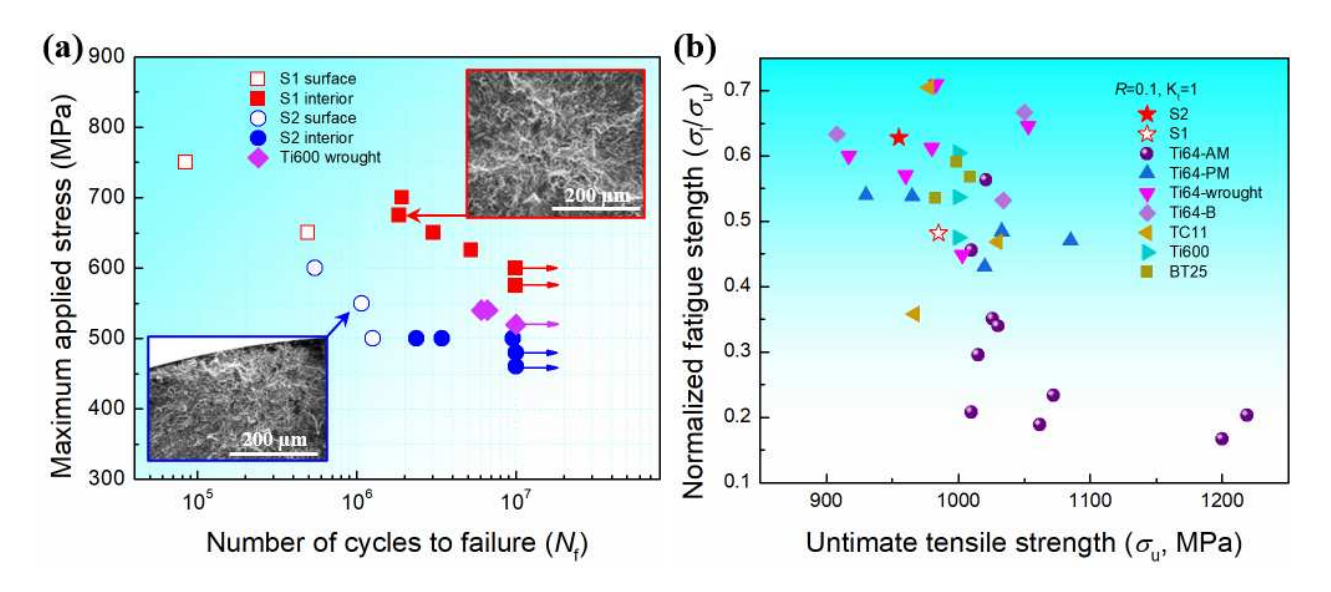


Fig. 3 Fatigue life and relationship between the fatigue and tensile strengths. (a) *S-N* curves of the HIPed Ti55 (surface: surface initiation; interior: interior initiation). The runout fatigue samples $(N_f > 10^7 \text{ cycles})$ are indicated by arrows. (b) Comparison of the properties of S2 with other high-temperature titanium alloys [17,19, 40–58], σ_u and σ_I standing for tensile and fatigue strengths, respectively. AM – additive manufacturing.

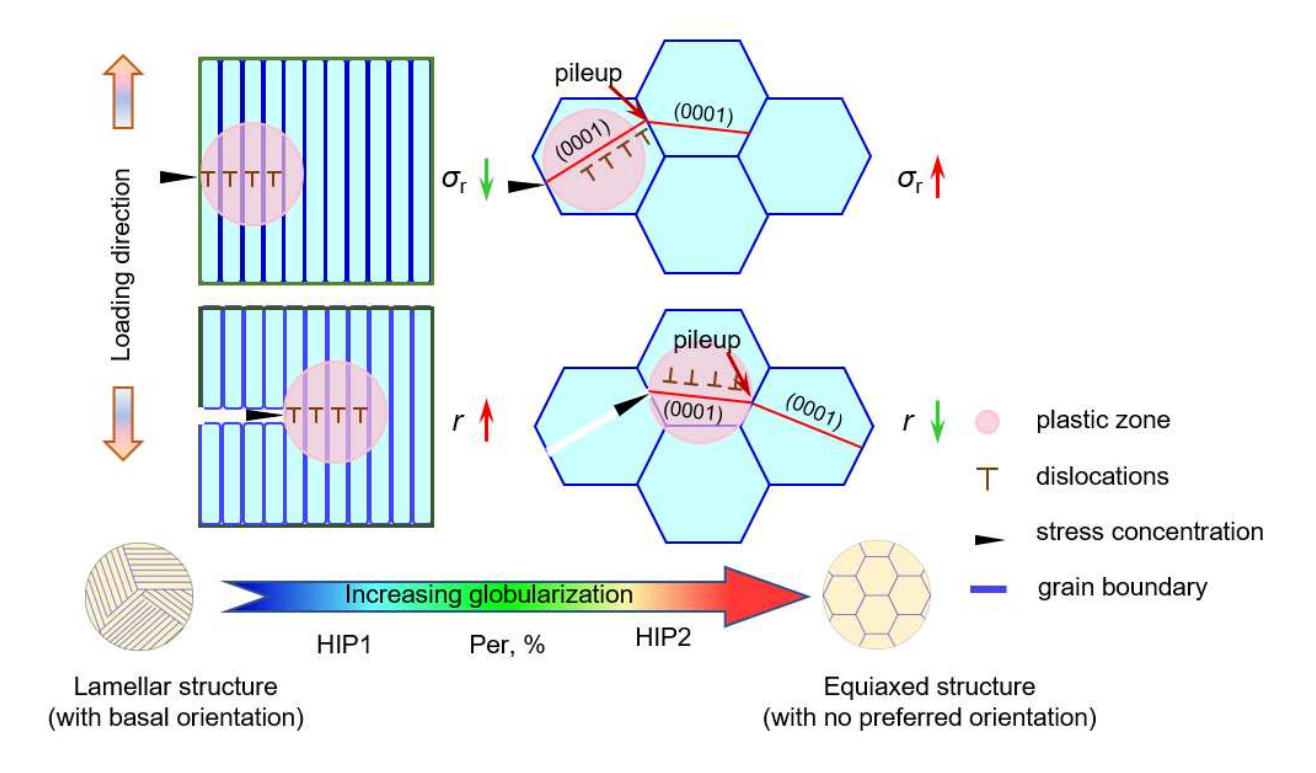


Fig. 4 Mechanistic schematic of fatigue-crack initiation. σ_r and r standing for the resistance for the crack nucleation and growth rate of short cracks, respectively and the arrows indicating their relative values.

Supplementary material

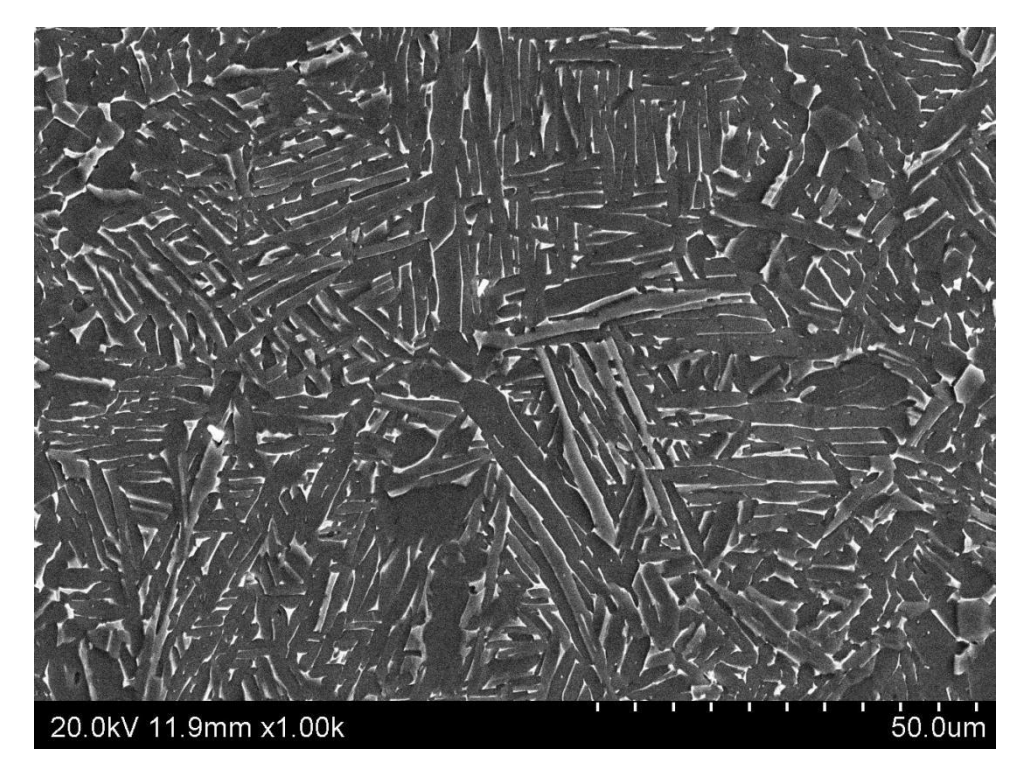


Fig. S1 SEM image showing the microstructure of the sample S1 after the first-step HIP of $880^{\circ}\text{C}/140\text{MPa/1h}$.

Table S1 Tensile properties of the Ti55 compact, using HIP1 and HIP2

HIP route	UTS (MPa)	YS (MPa)	El. (%)
HIP1	975±5	906±4	16.0±0.5
HIP2	955±5	881±2	16.5 ± 0.2

Note: UTS, YS, and El. stand for the ultimate tensile strength, yield strength, and elongation, respectively.

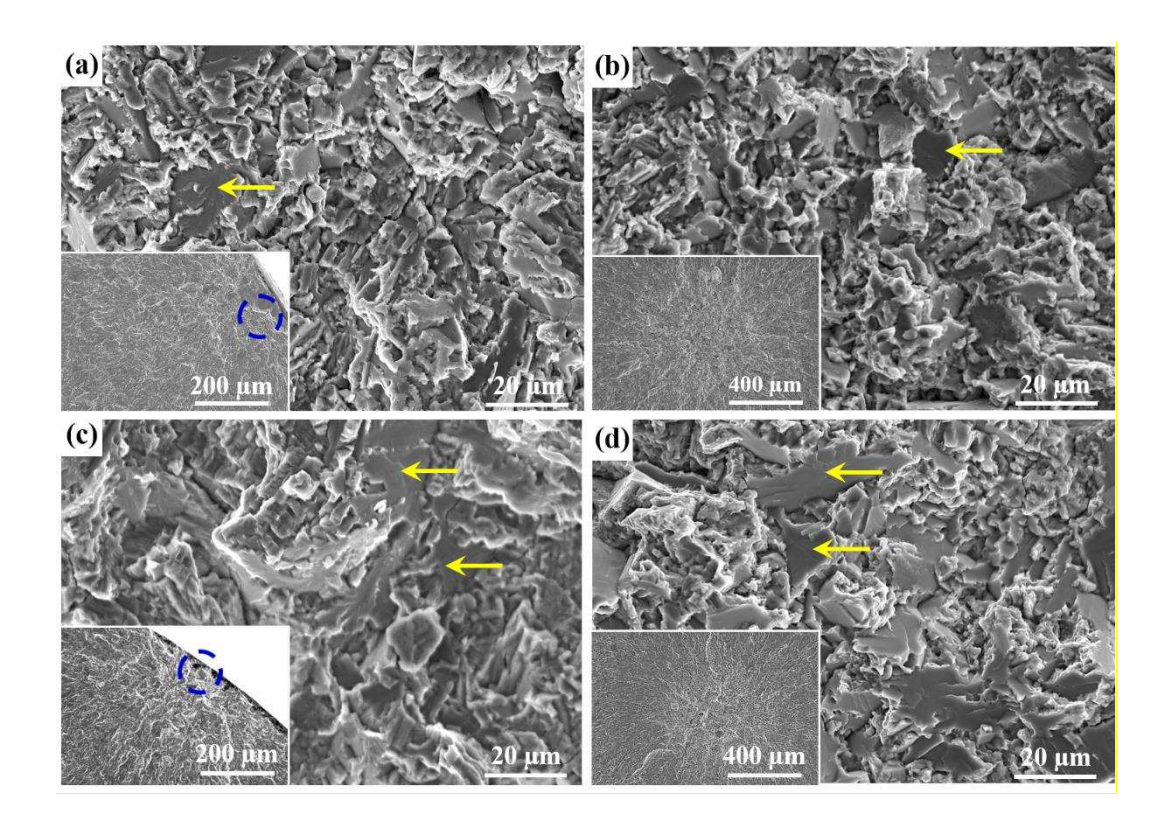


Fig. S2 SEM images showing the fatigue-fracture surface of the Ti55 alloy specimens: (a) HIP1 tested at $\sigma_a = 600$ MPa, $N_f = 5.47 \times 10^5$; (b) HIP1 tested at $\sigma_a = 500$ MPa, $N_f = 3.43 \times 10^6$; (c) HIP2 tested at $\sigma_a = 650$ MPa, $N_f = 4.95 \times 10^5$; (d) HIP2 tested at $\sigma_a = 625$ MPa, $N_f = 5.24 \times 10^6$, where the facets were indicated by the yellow arrows.

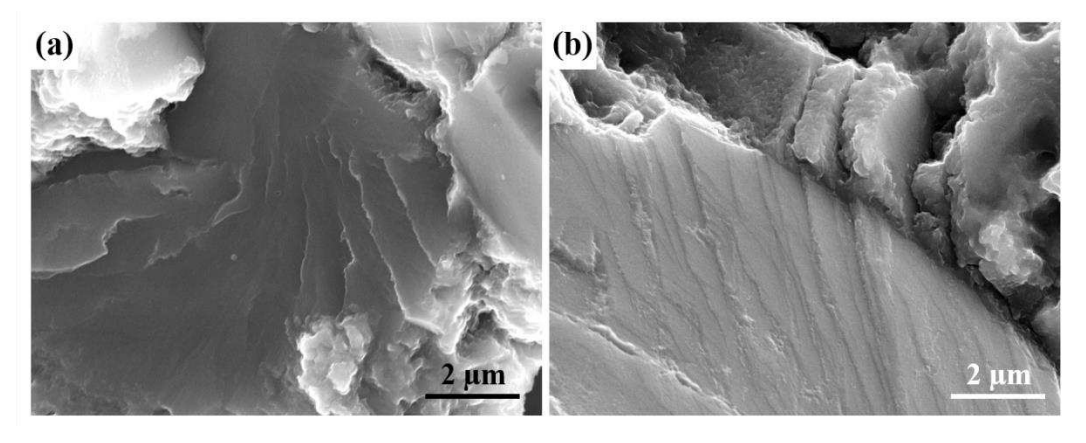


Fig. S3 High-magnification SEM images presenting the slip localization induced by cyclic loading at the facet surfaces of the failed Ti55 alloys. (a) HIP1 tested at $\sigma_a = 600$ MPa, $N_f = 5.47 \times 10^5$; (b) HIP1 tested at $\sigma_a = 500$ MPa, $N_f = 3.43 \times 10^6$. The striations reveal the slip steps on the facet surface under continuous cyclic loading, and the space of striation can be considered as the crack-growth rate.